Experimental and computational characterization of phase transitions in CsB_3H_8

Olena Zavorotynska*[1,2], Magnus H. Sørby[1], Jenny G. Vitillo,[3] Stefano Deledda[1], Christoph Frommen[1], Bjørn C. Hauback[1]

[1]*Department for Hydrogen Technology, Institute for Energy Technology, P.O. Box 40, NO-2027 Kjeller, Norway.*

[2] *Institute for Mathematics and Physics, University of Stavanger, P.O. Box 8600, NO-4036 Forus, Norway*

[3]*Department of Science and High Technology and INSTM, Università degli Studi dell'Insubria, Via Valleggio 9, I-22100 Como, Italy.*

*corresponding author: olena.zavorotynska@uis.no

Abstract

Metal hydroborates are versatile materials with interesting properties related to energy storage and cation conductivity. The hydrides containing $B_3H_8^-$ (triborane, or octahydrotriborate) ion, have been at the center of attention for some time as reversible intermediates in the decomposition of BH_4^- ($3BH_4^- \leftrightarrow B_3H_8^- + 2H_2$), and as conducting media in electrolytes based on boron-hydride cage clusters. We report here the first observation of two phase transitions in CsB_3H_8 prior to its decomposition above 230 °C. The previously reported orthorhombic room temperature phase (here named α-CsB_3H_8) with the space group *Ama2* changes into a new phase with the space group *Pnma* at 73 °C (here named β-CsB_3H_8), and then into a face-centered cubic phase, here named γ-CsB_3H_8, at 88 °C. These phases are not stable at room temperature thus requiring *in situ* measurements for their characterization. The phase transitions and decomposition pathway of CsB_3H_8 above 230 °C were studied with *in situ* synchrotron powder X-ray diffraction (SR-PXD), *in situ* and *ex-situ* vibrational spectroscopies (Raman and FTIR), and differential-scanning calorimetry combined with thermo-gravimetric analysis (DSC-TGA). The structure determination was validated by vibrational spectroscopy analysis and modeling of the periodic structures by density functional methods. In γ-CsB_3H_8, a significant disorder in $B_3H_8^-$ positions and orientations was found which can potentially benefit cation conducting properties through paddle mechanism.

Keywords: octahydroborate, triborane, borohydride, in situ synchrotron PXRD, in situ Raman, DFT, CRYSTAL17, solid-state electrolytes, hydrogen storage.

Introduction

Inorganic hydroborates is a very large class of compounds comprising an anion $[B_xH_y]^{z+}$ and a metal cation. Hydroborates have many uses, for example, in organic synthesis, catalysis, medical diagnostics, as liquid electrolytes, and as fuels.[1-4] The interest in boron hydride chemistry was strongly reinforced by search for hydrogen storage materials for hydrogen economy.[5-7] The compounds of the practical importance have been alkali, alkaline-earth and light transitional metal borohydrides ($M^{+x}(BH_4)^-_x$) with high gravimetric hydrogen densities. Magnesium borohydride $Mg(BH_4)_2$ is of particular interest for hydrogen storage. It was suggested to decompose via formation of a $B_3H_8^-$

intermediate.[8, 9] On the other hand, it is known that BH_4^- salts are the decomposition reaction products of $B_3H_8^-$ in the alkali metal salts.[10, 11] In this respect, the question of pyrolysis of $B_3H_8^-$ salts is of a particular interest since, if $B_3H_8^-$ decomposes to BH_4^-, it is unlikely that BH_4^- selectively decomposes to $B_3H_8^-$. It was in fact recently shown that an additional source of hydrogen is required for the selective $B_3H_8^- \rightarrow BH_4^-$ coversion.[12] In addition to attractive hydrogen-storage properties, high-temperature (H*T*) phase polymorphs have shown excellent ion-conducting properties.[13, 14] These ion-conducting properties can be preserved at lower temperatures if the conducting phase is stabilized at R*T* by, for example, ion substitution,[15-17] which paves the way to room-temperature solid state electrolytes with excellent ion conductivity.[14, 18]

The rich structural chemistry of inorganic hydroborates containing $[B_xH_y]^{z+}$ anions was recently reviewed by Černy et al.[19] The structure, hydrogen uptake, ion conducting properties of NaB_3H_8 [20-22] and KB_3H_8,[10] as well as novel synthesis methods for several octahydroborate salts[23] were described. In the case of KB_3H_8 (potassium octahydroborate), two new phases were reported in addition to the R*T* phase[10] and reorientational dynamics of $B_3H_8^-$ was studied with neutron scattering. [24]

Cesium octahydroborate, or triborane, (CsB_3H_8), has long been known among other borohydrates as a starting compound for the synthesis of higher boranes. Pyrolysis of CsB_3H_8 at 230ºC under vacuum affords good yields (60%) of CsB_9H_9 and is accompanied by the formation of $CsB_{10}H_{10}$, $CsB_{12}H_{12}$, $CsBH_4$ and hydrogen gas {Clark, 1968 #65}. The decomposition pathway was previously established primarily by mass spectrometry and nuclear magnetic resonance, whereas diffraction studies have not been carried out so far. Although the R*T* structure of CsB_3H_8 (referred to as α phase in this work) was reported in 1989 [25], no other phases have been observed so far.

In this work, we report on two new high-temperature phases of CsB_3H_8, here named β-, and γ-CsB_3H_8, which were observed by calorimetric studies and by *in situ* synchrotron X-ray diffraction. The structures of the two new phases, β-, and γ-CsB_3H_8, were determined by Rietveld refinement of the diffraction data. The experimental analysis was supported by periodic Kohn-Sham density functional (KS-DFT) calculations. The vibrational properties of $B_3H_8^-$ were analyzed basing on the calculated spectra and on the crystal field splitting.[26] The phase transitions were also characterized by *in situ* Raman spectroscopy.

Materials and Methods

CsB_3H_8 was purchased from Katchem and stored in Ar-filled glovebox. **Synchrotron powder X-ray diffraction (PXRD)** studies were performed at the ESRF-SNBL synchrotron radiation facility, at the beamline BM01A using a 0.681630 Å wavelength and a 2D Pilatus detector. For the *in situ* measurements, as received CsB_3H_8 powder was placed in a 0.5 mm boronglass capillary and heated by an air blower to 570 °C at the 5 °C/min under a dynamic vacuum. The PXRD patterns were recorded every 10 sec, during which the capillary was rotated by 10°. The temperature of the air blower was calibrated from the melting points of In, Sn, and Zn standards. Additional data were obtained at selected temperatures at BM01B with a CMOS detector using a wavelength of 0.505131Å. For these measurements, the 0.5 mm boronglass capillary was spinning rapidly during data acquisition. The 2D diffraction images were integrated with Fit2D software, using LaB_6 powder from NIST as the calibration standard for the sample-to-detector distance. The patterns were analyzed by simulated annealing and Rietveld refinements using Topas Academic version 6. [27]

Differential scanning calorimetric combined with thermogravimetric (DSC-TGA) measurements were performed with a Netzsch STA 449 F3 Jupiter instrument. Samples were measured in

Al_2O_3 crucibles with pierced lids at a heating rate of 5 °C min in a 50 ml/min Ar flow. CsB_3H_8 was heated in the R*T* – 575 °C range in one study. In the second study, the compound was heated stepwise to 200, 231, 450, and 600 °C. The reaction products after each step were analyzed with SR-PXD, IR, and Raman spectroscopies.

Raman scattering spectra were obtained with the REINSHAW inVia Raman Microscope. The spectra of the powders sealed in the glass capillaries were obtained with a 532 nm excitation wavelength in the 4000-50 cm^{-1} spectral region.

Attenuated total reflection Fourier transformed infrared (ATR FTIR) spectra were measured with a Bruker Alpha-Platinum infrared spectrometer (internal reflection element in diamond). The spectra were obtained in the range of 4000-375 cm^{-1}, with a resolution of 2 cm^{-1}, with 32 scans averaged for each spectrum and the background. The samples were measured without any dilution. All the IR measurements were conducted in an argon-filled glove box with exception of the measurements of hydrated samples that were collected in air. Hydrated samples for the infrared study were obtained by wetting a sample slightly with distilled water. The subsequent partial dehydration was achieved leaving the sample in a fume hood at *R*T in air and taking the spectra during the day. The complete dehydration was achieved after degassing the sample in dynamic vacuum at 120 °C overnight.

DFT calculations have been performed using the CRYSTAL17 program[28] by means of the Becke's three-parameters hybrid exchange functional[29] supplemented with the Lee, Yang, and Parr's gradient-corrected correlation functional[30] (hereafter B3LYP). All-electron Gaussian type basis sets of triple-ζ valence quality were adopted for B and H atoms. For the Cs atoms, the ECP46MDF basis set and the corresponding energy-consistent, relativistic pseudopotentials have been used.[31, 32] From the original ECP46MDF basis set, the two diffuse orbitals have been removed.

Three phases of the CsB_3H_8 have been considered: α, β, and γ. Both lattice parameters and atom positions were fully optimized, if not otherwise specified, by keeping the initial space group symmetry fixed. The crystallographic unit cells used in the calculations contain four formula units ($Cs_4B_{12}H_{32}$). For β and α phases, the same space group observed experimentally was adopted (*Ama*2 for α and *Pnma* for β) and the Rietveld refined structures were used as the starting geometry. *Gamma*-phase is characterized by a high symmetric structure with many partly occupied B- and H-sites which represent the average of different orientations of the $[B_3H_8]^-$ units. In the calculations, it was not possible to consider a partial occupation of crystallographic sites. The input structure was constructed from the experimental one orienting the $[B_3H_8]^-$ present in the cell randomly. This cell contains four formula units and the space group is P_1. It was verified that the initial orientation of the borohydrate units does not influence the final relaxed structure.

For numerical integration of the exchange-correlation term, a (75 974) pruned grid was adopted.[33] The threshold conditions for convergence in self-consistent field (SCF) iterative procedure was set to 10^{-8} and 10^{-10} hartree for geometry and frequency calculations, respectively. The Pack−Monkhorst/Gilat shrinking factors for the reciprocal space were set to 8 and 8, corresponding to 260 and 260 points at which the Hamiltonian matrix was diagonalized. The accuracy of the integral calculations was increased by setting the tolerances to 7, 7, 7, 7, and 25. To accelerate convergence in the SCF process, a modified Broyden's scheme,[34] following the method proposed by Johnson,[35] was adopted. The method was applied after 5 SCF iterations, with 70 % mixing of the Fock/Kohn–Sham (KS) matrices and the Johnson's parameter set to 0.05. The above computational parameters ensured full numerical convergence on all computed properties described herein.

Vibrational frequencies at the Γ point and their IR and Raman intensities were calculated on the optimized geometries by means of a mass-weighed Hessian matrix, obtained by numerical differentiation of the analytical first derivatives.[36] Infrared and Raman intensities were calculated via an entirely analytical procedure based on a linear response.[37, 38] A Lorentzian broadening of 5 cm^{-1} was adopted for Raman spectra while a Gaussian broadening of 5 cm^{-1} was adopted for the IR spectra. No scaling factors have been applied to the calculated values of the vibrational modes.

Results and Discussion

1. Phase-transitions in CsB_3H_8

The DSC-TGA studies of CsB_3H_8 in 22 ─ 565 °C temperature range showed several temperature-induced events (Fig. 1a). Below 200 °C, four endothermic peaks (T_{ons} = 74, 102, and a doublet at 140-160 °C) with a total weight loss of 2.60 % were observed. The nature of those peaks was clarified in the further heating → cooling → heating cyclic studies within the same temperature range (Fig. 1b). Only the first two peaks at T = 74 - 108 °C were reproducible during all the heating and cooling stages and were therefore assigned to phase transitions in CsB_3H_8 (Fig. 1b). No weight loss was associated with these peaks upon heating. The double DSC peak observed at T = 140-160 °C in Fig.1a and the corresponding weight loss of 2.60 % were assigned to desorption of impurities (most probably, $Cs(B_3O_5)\cdot xH_2O$ as indicated by pattern library search). The subsequent *in situ* SR-PXD data, shown in Fig.1c, clearly demonstrated two phase transitions before decomposition of the sample above 200 °C and at temperatures very close to those observed in the DSC experiments. In particular, the diffraction peaks from the R*T* phase of CsB_3H_8 disappeared after 75 °C, and a new phase, denoted as *phase I*, was formed. *Phase I* was transformed to *phase II* at 109 °C. The weak diffraction peaks assigned to $Cs(B_3O_5)\cdot xH_2O$ vanished at 144 -168 °C.

Further, the analysis of *ex-situ* XRD and FTIR data of the samples heated up to 200 °C (Fig. 2) showed that:

i) the FTIR spectrum (Fig. 2a) and XRD pattern (Fig. 2b) of the sample heated in Ar until 200 °C, both recorded *ex-situ* and at room temperature, were very similar to those measured on the as-received sample with the exception of a decrease of intensity of the broad peaks around 3500 and 1500 cm^{-1} in FTIR spectra and of the weak peaks due to the impurities in the XRD patterns. This clearly indicated that *phase II* reverted to the R*T*-modification on cooling. This is also confirmed by different XRD patterns obtained *in situ* at 200 °C (Fig. 2c) and *ex-situ* after heating to 200 °C (Fig. 2b).

ii) The *ex-situ* FTIR spectra and XRD patterns of the samples resulting from thermolysis at 253-450, and 575 °C were significantly different from those of the as received sample and the one obtained after thermolysis at 200 °C indicating at least two-steps in the decomposition of CsB_3H_8: at ca. 250 and 570 °C.

iii) The XRD pattern of the sample after thermolysis at 575 °C shown in on the Fig. 2b differs from the one obtained at 570 °C *in situ* (see Fig. 2c). This can be explained by phase-transitions occurring in the decomposition phases, different decomposition pathways depending on the condition of decomposition reactions (in this case, in Ar and in dynamic vacuum for the *ex-situ* and *in situ* measurements, respectively), or additional decomposition steps around that temperature not captured in one of the experiments.

Additional FTIR study, presented in the SI (Fig. S1), shows the correlation of the FTIR peaks around 3500 and 1500 cm^{-1} with water content in the sample. This study was carried out with the purpose to identify the water-related products in the FTIR spectra. Notably, water can be removed from the CsB_3H_8 upon heating in air and eventually in vacuum at 120 °C.

Thus, two new modifications of CsB_3H_8 were observed in in situ SR-PXRD and DCS-TGA measurements, and both the *ex-situ* XRD patterns and FTIR spectra indicated that these high temperature polymorphs were not preserved upon cooling to R*T*.

2. Decomposition of CsB_3H_8

Decomposition of CsB_3H_8 was observed in the TGA-DSC data as a strong exothermic peak and a 1.88% weight loss in the 212-244 °C temperature range (Fig. 1a). The initial decomposition products were stable up to 490 ˚C, after which they further decomposed with a weight loss of ca. 5 wt%. The FTIR spectra and XRD patterns of the reaction products, obtained *ex-situ* after each reaction steps, confirmed the formation of new phases. The *in situ* SR-XRD patterns recorded above 203 ˚C also confirmed the changes in the crystalline phase composition of the sample. In particular, *phase II* disappeared in favor of several new phases. One of them, *phase III*, was stable up to 460 °C, and subsequently transformed into another crystalline compound(s), *phase IV*. Another phase, *V*, formed at/above 203 °C was stable up until the end of the measurement at 570 °C.

Hydrogen comprises 4.6 wt% of pure CsB_3H_8. Disregarding the initial 2.6 wt% weight loss as release of impurities, it can be inferred that the weight loss during the first decomposition step was 1.9 wt%. Desorption of diborane B_2H_6 during the first step can be ruled out as this would had resulted in a weight loss of almost 16 wt% with respect to pure CsB_3H_8. Thus, it can be concluded that the main gaseous product of the first decomposition reaction is H_2. The second decomposition step resulted in at least 5 % weight loss thus suggesting the desorption of volatile reaction products other than H_2.

3. Crystal structure of polymorphs

3.1 SR-PXD

The SR-PXD data collected at SNBL BM01 with a Pilatus detector had clearly issues with preferred orientation due to the small rotation of the capillary during data acquisition, and structure analyses were therefore performed with data collected from spinning capillaries with the CMOS detector at SNBL BM01B.

The Rietveld refinement of the R*T* phase of CsB_3H_8 is shown in the ESI, Fig. S2, and the *phase I* and *phase II* are depicted in the Fig. 3. Rietveld refinement of the R*T* phase was performed with the previously reported structure as a starting point. Soft constraints were put on bond-distances and angles in the B_3H_8 unit and weighted so that the distances agreed within 0.02 Å and angles within 5° of those found by DFT. An excellent fit was obtained with minor changes in the structure model compared to the previous report (Fig. S2).[25]

The structures of the high-temperature phases were solved ab-initio. Indexing in Topas indicated an orthorhombic unit cell for the *phase I* and systematic extinctions suggested *Pnma* space group symmetry. Structure solution was performed with simulated annealing in Topas where the B_3H_8 unit was treated as a rigid body. Subsequent Rietveld refinement was performed with soft constraints, similar to the R*T*-refinement, rather than rigid body description of B_3H_8. The final fit to the experimental data is shown in Fig. 3a.

Phase II was indexed according to a face-centered cubic unit cell. Rietveld refinements were performed assuming a NaCl-type structure (space group *Fm*-3*m*) with Cs in one site (4*a)* and orientationally disordered B_3H_8 on the other site (4*b*), similar to H*T*-KB_3H_8.[10] A non-scattering reference atom was placed in the 4*b* site and B, H1, and H2 were placed in general positions (192*l*) 1.05 Å, 1.55 Å and 1.96 Å from the reference atom, corresponding to the distances from the center of the B_3-triangle to the three B, the two bridging H atoms and the six terminal H atoms, respectively. The occupancies were adjusted to get 12 boron atoms in the B site, 8 H atoms in the H1 site and 24 H atoms in the H2 sites. The distances where soft constrained to not change more than ±0.02 Å. During Rietveld refinements, the B atom moved very close to a 48*i* position while both H atoms moved close to 96*k* positions. The atoms where thus put in these positions and the occupancies were adjusted accordingly. The Cs atom got at very high displacement factor (B_{iso} = 21 $Å^3$), similar to what Griderslev et al. reported for the HT-structure of KB_3H_8.[10] They revised their structure based on quasi-elastic neutron scattering data, and moved the K^+ slightly away from 4*a* to a partly occupied general site.[24] The same approach was adopted in this work for the refinement of the *phase II* which led to a better fit (Fig. 3b) and a more sensible displacement parameter for Cs^+. The cation moved close to a 96*k* position, where it was placed in the final refinement.

The R*T* phase of CsB_3H_8 and the *phases I* and *II* were thus named *α*-, *β*-, and *γ*-CsB_3H_8, respectively.

3.2 Periodic DFT calculations.

The DFT calculations provided the order of stability expected based on the different temperature at which each phase was observed: *α* resulted the most stable phase, while *β* and *γ* appeared to be higher in energy of 0.7 and 9.9 kJ mol^{-1} per formula unit, respectively.

A very good agreement between the experimental and the DFT optimized cell parameters was obtained for *α*- and *β*-CsB_3H_8, as shown in the Table 1. The calculated R*T* structure agrees with the experimental structure also with respect to the atomic positions. The optimization starting from the experimental atomic positions ended up in a structure where the B_3H_8 units were restored. A good agreement was also obtained for the calculated Raman and IR spectra frequencies (see Section 3.3 and Fig. S3).

The direct comparison between DFT and experiment for *γ*-CsB_3H_8 is make difficult by the difference between the model and the real system (see Materials and Methods). An optimization allowing a full relaxation of both the lattice parameters and the atom positions ended up in a unit cell having parameters significantly different from the experimental ones (*a* = 8.905, *b* = 7.340, *c* = 9.137 Å versus *a* = *b* = *c* = 8.44 Å, respectively). This was due to the preferential alignment of all the $B_3H_8^-$ units in the *xz* plane in the calculated structure, instead to be averaged equally among four directions as in the experiments (and none of them coincident with the *xz* plane). The density of the calculated structure was essentially coincident with the experimental density. This theoretical structure has a simulated XRD pattern significantly different from that of the experimental one. The optimization was then performed by keeping the unit cell parameters fixed to the experimental values. The increase in energy of the R*T* structure so optimized with respect to the fully relaxed one was very small (5.3 kJ mol^{-1} per formula unit). In this case, the simulated XRD pattern agree with the experimental one, while the theoretical Raman and IR spectra are showing a significant larger number of peaks than the experimental spectra, due to the lower symmetry of the model (*Fm*-3*m* versus P_1: see Section 3.3 and Fig. S3).

3.3. Vibrational properties of CsB_3H_8 phases

Raman, FTIR, and inelastic neutron scattering spectra of CsB_3H_8 were reported and tentatively assigned before by Tomkinson et al.,[26] however, without taking into consideration the crystal field splitting in then unknown crystal structure. Here we present the analysis of the vibrational properties of CsB_3H_8 in *Ama2* (C_{2v}) crystal field. The calculations of vibrational frequencies were performed on the primitive cell with Z=2.

Molecular ion $B_3H_8^-$ has C_{2v} symmetry[39] and 27 normal modes of vibrations. These can be represented as $\Gamma_{B3H8}^{ion} = 9A_1 + 5A_2 + 6B_1 + 7B_2$.[40] In the CsB_3H_8, the site symmetry of $B_3H_8^-$ is reduced to C_s. Crystal field splitting (C_{2v}) in the primitive cell with Z = 2 gives rise to total of 54 vibrations of $B_3H_8^-$ excluding the rotational and translational modes. These are transformed, according to the correlation rules shown in the Table 2, as $\Gamma_{B3H8}^{cryst} = 15A_1 + 12A_2 + 15B_1 + 12B_2$. The total reducible representation for the unit cell of α-CsB_3H_8, including translations of Cs atoms, is expressed as $\Gamma_{total} = 20A_1 + 16A_2 + 16B_1 + 20B_2$. Out of these, $A_1 + B_1 + B_2$ represent acoustic modes.[41] Thus, the lattice modes (rotations and translations of the two $B_3H_8^-$ = 12 modes, translations of Cs = 3 modes) can be written as $\Gamma_{lattice} = 4A_1 + 4A_2 + 7B_2$. All the modes are fundamentally Raman-active, those with A_2 symmetry are silent in infrared.

Fig. 4 shows the comparison of the experimental and calculated B-H stretching region for the α-CsB_3H_8. Peak assignment is summarized in the Table 3. The modes are numbered according to the calculated peak positions. The DFT calculations significantly overestimate the energy of B-H stretching vibrations whereas the computed bending modes are in a much better agreement (Fig. 5). This is a common trend in H-containing molecular solids, and it is associated to the larger anharmonic character of stretching than bending modes (for examples on borohydrides, see Refs. [42, 17, 43])

Sixteen *B-H stretching modes* can be expected: $\nu_1 - \nu_{16}$. They are clearly divided into two regions separated by about 200-300 cm^{-1}: the twelve modes due to the stretching of the terminal (BH_{term}) and four modes due to the two bridging (BH_{br}) H atoms in the 2540 – 2250 and 2190 and 1990 cm^{-1}, respectively (experimental data). In $B_3H_8^-$, there are two types of terminal hydrogens: those at B1 (4 H atoms) and at the B2 (2 H atoms) (Fig. 4 and Table 3). All the terminal H are located out of the B-B-B plane. Two stretching modes are expected for the B2-H_{term} (symmetric, A_1, asymmetric, B_1), and the crystal field splitting results in four of those modes (($A_1 + B_1$) and ($A_1 + B_1$)). For the B1-H_{term} group, one in-phase symmetric stretching, $\nu_{s\text{-}in}$, (A_1), one out-of-phase symmetric, $\nu_{s\text{-}out}$, (B_2), one in-phase asymmetric, $\nu_{as\text{-}in}$, (B_1), and one out-of-phase asymmetric, $\nu_{as\text{-}out}$, (A_2), modes are expected each split into two due to the crystal field. In the solids containing BH_4^- ions, the totally symmetric stretching of terminal H atoms has a lower energy than the asymmetric stretching.[7, 40, 43, 44] A similar trend can be seen here according to the calculations: ν_{as} (B2-H_{term}) shifted by 30 cm^{-1} to the higher frequencies compared to the ν_s (B2-H_{term}) and the symmetric and asymmetric modes for B2-H_{term} stretching demonstrate the same trend. The BH_{br} modes represent in-phase and out-of-phase stretching of the two B2-H-B1 groups as shown in Fig. 4 with black and red arrows, respectively. Here, the in-phase stretching is larger in energy than the out-of-phase motion by almost 40 cm^{-1}. The computed crystal field splitting is small for the BH stretching modes reaching at most 10 cm^{-1}. Besides, there is a significant out-of-phase coupling between $\nu_{s\text{-}in}$ (B1-H_{term}) and ν_s (B2-H_{term}).

In the IR spectrum, the most intense feature in the higher-energy region is found at 2467 cm^{-1} and can be assigned to the asymmetric stretching (B_1) of B2-H_{term} (ν_2) by comparison with the computed

infrared intensities. In the Raman spectrum, its counterpart could be suggested at the same position, 2467 cm^{-1} having the A_1 symmetry (v_1). In the following, the peaks in the Raman spectrum are assigned mostly to the symmetric modes whereas those in the FTIR spectrum are assigned to the asymmetric modes. The most intense Raman peak at 2454 cm^{-1} was assigned to the symmetric, A_1, B2-H_{term} stretching. It has also the highest intensity in the calculated spectra (v_4 at 2541 cm^{-1}) and does not have a distinguishable counterpart in FTIR. The B_1 component of this vibration (v_3) is thus considered to be too weak both in Raman and IR. The asymmetric stretching modes of B1-H_{term} groups are grouped around a shoulder at 2530 cm^{-1}. The $v_{as\text{-}out}$ (B1-H_{term}) has a very low calculated FTIR intensity for the B_2 component whereas the A_2 component is IR-inactive. At the same time, the $v_{as\text{-}in}$ (B1-H_{term}) has a very high predicted IR intensity. In the experimental Raman spectra, a doublet can be observed at 2416 and 2406 cm^{-1} whereas only one peak is observed in this area in the IR. Thus, the Raman doublet is assigned to the $v_{as\text{-}in}$ (B1-H_{term}) and $v_{as\text{-}out}$ (B1-H_{term}), whereas the singlet at 2405 in the FTIR spectra is assigned to the $v_{as\text{-}in}$ (B1-H_{term}). The remaining peaks in the spectra were assigned to the symmetric stretching of the B1-H_{term} and in-phase and out-of-phase B2-H-B1 groups.

In the experimental Raman spectrum, a weak feature, which is marked with an asterisk in the Fig. 4, is visible at 2226 cm^{-1} between regions for terminal (BH_{term}) and bridging (BH_{br}) H atoms. In the earlier work,[26] this peak was assigned to the v_3 (A_2) fundamental. In our calculated spectra, however, there are no features between the BH_{term} and bridging BH_{br} regions. Therefore, we suggest to re-assign this feature to an overtone of a bending mode. The position of this overtone at 2226 cm^{-1} matches well with the peak of a fundamental mode at 1111 cm^{-1}. Thus, about half of the predicted frequencies were observed in the experimental spectra in accordance with the calculated very small crystal filed splitting. In this analysis, The B^{10}-B^{11} splitting was not taken into consideration due to the rather broad experimental peaks. The isotopic splitting mostly affects the modes involving large displacements of boron atoms. The anharmonicity and Fermi resonance are known to add to the complexity of the experimental spectra of borohydrides (containing BH_4 cm^{-1} ions),[42] and cannot be fully ruled out here.

Most of the spectral features in the low-frequency region, shown in Fig. 5, involve motions of most atoms in the $B_3H_8^-$ anions. The calculated IR and Raman spectra represent the experimental spectra very well and thus the features were assigned by direct comparison of the computed and experimental intensities. In the experimental Raman spectrum, the most distinguishable features are assigned to the symmetric stretching of the B-B-B rings at ca. 800 cm^{-1}. This mode has a very weak intensity in the IR. The intensity of the asymmetric stretching mode both in IR and Raman is very weak. The motions involving the librations of the whole $B_3H_8^-$ anions were computed below 185 cm^{-1}, and those involving Cs and $B_3H_8^-$ translations were predicted below 100 cm^{-1}. A full list of the modes and of their assignment to atomic displacement is reported in Table 3.

The phase transitions in CsB_3H_8 were followed by *in situ* Raman spectroscopy. During phase transitions, the changes in geometry and local environment of $B_3H_8^-$ should be reflected in the vibrational spectra. Indeed, substantial changes were observed in the B-H_{term} stretching region (Fig. 6). Here, apart from the temperature-related broadening of the peaks, which was also characteristic for the rest of the spectra, we observed the rapid decrease in intensity of the peaks centered around 2412 cm^{-1} and assigned to the asymmetric stretching of B1-H_{term}. This was accompanied by decrease in the intensity of the bending modes of this group, in particular the v_{22} at 1214 cm^{-1}. Thus, a considerable contribution of the overtones of the bending modes in the stretching region at ca. 2410 cm^{-1} is plausible. The v_4 and v_{22} modes, assigned to symmetric stretching and bending of terminal H atoms at B2, were observed to shift to lower energies, i.e., 2453→2442→2431 for v_4 and 1214→1208→1201 cm^{-1} for v_{22} at R*T*, 88 and 111 °C,

respectively, indicating changes in the geometry of this group (e.g, bond elongation). According to the refined experimental structures, the B2-H4 bonds are the only ones that underwent slight elongation upon the first phase transition (Table 4). Thus, we suggest that this can be associated with the red shift in the v_4 and v_{22} modes assigned to the groups containing this bond. However, these differences, should be interpreted with caution due to the weak scattering from hydrogen and the elongation within the uncertainties. The position of the v_{27}, associated mostly with bending of bridged hydrogen atoms δ_{twist} (B-H_{term} + BH_{br}) and some contribution from the B-H_{term}, along with the stretching modes for the bridged B-H-B groups, did not change the position during the phase transitions. In addition, the intensity of the v_{27} decreased in accordance with the intensity of the peak at 2226 cm^{-1}, earlier assigned to $2v_{27}$, as expected. The relative intensity in the v_{39} mode associated with B-B-B ring asymmetric deformation, significantly decreased already in β-phase. Besides, a significant broadening upon phase transition was observed in the peak at 133 cm^{-1}. This could be explained if the peak is assigned to $B_3H_8^-$ libration modes (computed below 185 cm^{-1}) and orientational disorder of the $B_3H_8^-$ anions in the H*T* phases.

As mentioned above, the B3LYP structure for the γ-phase is significantly different from the experimental one. The calculated structure has a lower symmetry (*P*1 vs. *Fm*-3*m*) and a different orientation of the B_3H_8 units, which is along the *xz* plane in the calculated structure, whereas the orientation of the B_3H_8 units is thermally averaged in all directions in the experimental structure. The γ-phase is in fact a high symmetric structure where both H and B positions have an occupancy ≤ 0.25. This is likely associated with the high temperature (111 °C) that increases the thermal energy of the atoms, resulting in orientation disorder of the B_3H_8 units in the γ phase. The calculated spectrum for the γ-phase is significantly different from the experimental one (see Fig. S3a) and, as expected from the low symmetry of the calculated structure, shows a larger number of bands.

Calculated IR spectra have been obtained to help further investigation on the phase transitions in CsB_3H_8. The calculated IR spectra are reported in Fig. S3a. Interestingly, IR spectra for α-CsB_3H_8 and β-CsB_3H_8 phases are significantly different, both in the mid-IR and in the far-IR. Based on these results, IR spectroscopy is suggested as the most suitable spectroscopic technique to study *in situ* phase transitions in CsB_3H_8.

3.4 Decomposition products

Fig. 2c demonstrates that CsB_3H_8 decompose at ca. 203 °C and, after this event, the phase composition is unchanged up to 460 °C (*phase(s)* III). It was reported {Clark, 1968 #65} that decomposition of CsB_3H_8 at 230°C under vacuum yields 60% of CsB_9H_9 accompanied by some $CsB_{10}H_{10}$, $CsB_{12}H_{12}$ and $CsBH_4$. $CsB_{10}H_{10}$ is stable up to 600°C, and $CsB_{12}H_{12}$ at 810°C. $CsB_{11}H_{11}$ is converted to an equimolar mixture of $Cs_2B_{10}H_{10}$ and $Cs_2B_{12}H_{12}$. In an alternative decomposition pathway, $CsBH_4$ + CsB_6H_6 + H_2 were suggested to form. [45, 46] The other octohydroborates of alkali metals were reported to follow the decomposition reactions:

$NaB_3H_8 \rightarrow NaBH_4 + Na_2B_{12}H_{12} + Na_2B_{10}H_{10}$ + impurities (stoichiometry not given [11])

$5KB_3H_8 \rightarrow 3KBH_4 + K_2B_{12}H_{12} + 8H_2$, where the solid products of the reaction further reacts to form $K_3(BH_4)(B_{12}H_{12})$ [10]

Interestingly, the experimental PXRD patterns did not match with the available structures of the Cs hydroborates, i.e, $Cs_2B_6H_6$, and $Cs_2B_{12}H_{12}$, CsB_9H_{14} as summarized by Cerny et al.(ref) No similarities where also found with the patterns of $RbB_{10}H_{10}$. The most suitable reference compounds were found to be $CsBH_4$ and c-$K_3BH_4B_{12}H_{12}$ in the both *in situ* and *ex-situ* data obtained *at* 245 °C and *after* decomposition at 450 °C. In fact, most of the peaks in the experimental patterns could be explained by the two phases (see Fig. S4). Given the smaller size of the K cations, it could be suggested that the Cs hydroborate in question should contain a smaller closoborane ion, perhaps $B_6H_6^{2-}$ or $B_{10}H_{10}^{2-}$. On the contrary, the *ex-situ* PXD pattern recorded on the sample decomposed at 253 °C as well as both the *in situ* and *ex-situ* patterns of the sample decomposed at and after 575 °C contain unknown peaks and call for further investigation.

Some of the decomposition products for CsB_3H_8 are obviously crystalline (Fig. 2c), but some can be amorphous, as can be seen from elevated background on the Fig. 2b,c, and thus were also analyzed by FTIR (Fig. 7a). The broad absorption in the 2440 – 2540 cm^{-1} region can correspond to any of the $B_nH_n^{2-}$ (n = 6,8,9,10,11,12) anions.[47] $Cs_2B_9H_9$ was observed to produce four peaks in the IR in the B-H stretching region at liquid nitrogen temperature, namely at 2529, 2450, and 2415 cm^{-1}.[47] At room temperature we would expect the peaks to broaden. Fig. 7a shows that although the two latter peaks can be inferred from the broad absorption at ca. 2450 cm^{-1}, the presence of the first peak as 2529 is not that obvious, questioning the presence of $B_9H_9^{2-}$ anions in the sample. The FTIR fingerprint for $B_{12}H_{12}^{-}$ anions consists of the features at 2485 (strong, s), 1071 (m), and 719 (m) cm^{-1}.[48] Out of these, the first and the last peaks with low intensity can be clearly observed in the pattern obtained after thermolysis at 575 °C, whereas the peak at 1071 cm^{-1} can be part of the complex absorption region at 1200 – 1000 cm^{-1}. Thus, it can be suggested that $Cs_2B_{12}H_{12}$ was formed at the decomposition step above 500 °C and forms a part of *phases IV*, as described in Chapter 2. The weak reflections of the $Cs_2B_{12}H_{12}$ were found also in the correspondent PXD patterns as discussed above. Infrared spectra of $B_{10}H_{10}^{2-}$ salts have a very strong absorption at 2470 cm^{-1} (equatorial B-H stretch) with a shoulder at 2530 cm^{-1} (apical B-H stretch). A strong absorption at 1015 cm^{-1} and a weaker one at 1070 cm^{-1} were attributed to cage deformational modes {Clark, 1968 #65}. The peak at 1015 cm^{-1} can be clearly observed in the spectra of the sample obtained below 575 °C whereas the other peaks coincide with those of $B_{12}H_{12}^{2-}$. This peak at 1015 cm^{-1} disappeared at the second decomposition step. Closo-boranes $B_nH_n^{2-}$ (n = 6,8,9,10,11,12) do not have peaks in the region 1200 and 2500 cm^{-1},[47] thus, those features in the IR spectra, especially pronounced in the spectrum of the sample treated at 575 °C, might be explained by other classes of boranes. Characteristic modes of $B_6H_6^{-}$ could be observed in the spectra of all decomposed samples (F_{1u} modes at 2432, 1051, and 731 cm^{-1} in ref. [48] and at 2432, 1058-1048, and 734 cm^{-1} as shown on Fig.7a). Thus the FTIR data seem to indicate that the Cs compound in the samples after the first decomposition step contain both $B_6H_6^{2-}$ or $B_{10}H_{10}^{2-}$.

The FTIR spectrum obtained for the compound heated to 450 °C clearly showed the peaks due to $CsBH_4$ (peaks 2332, 2244, 2197, 2179, 1111, 1094 cm^{-1})[49] in addition to other phases. Crystalline $CsBH_4$ was also identified in the XRD patterns and was stable up to 460 °C as indicated by the *in situ* PXD. The origin of the pronounced features in the broad region 1600 – 1100 cm^{-1} most evident in the spectrum of the sample decomposed at 575 °C remains unknown. It may indicate the presence of the B-O groups.(ref)

Various gaseous boranes were detected in the decomposition of NaB_3H_8 [21] in addition to BH_4^{-} and $B_{12}H_{12}^{-}$ solid-state species. In these experiments, however, the insignificant weight loss did not indicate the release of gaseous boranes in stochiometric quantities although the weight loss was higher than that expected from the release of pure H_2. It might be suggested that the gaseous boranes reacted immediately with the solid reaction products to form other hydroborates.

In situ PXRD and Raman experiments indicated a slightly lower decomposition temperature, as crystalline $CsBH_4$ was observed already around 200 °C. The *in situ* Raman spectra have registered numerous new phases that were formed already at 190 °C and existed only for 20 minutes (Fig. 7b) at the constant temperature before changing into the mixture containing $CsBH_4$. The difference in the decomposition temperatures can be explained by temperature calibration of the Raman set-up and kinetics of the decomposition reaction as the phase-transition temperatures in PXRD and DSC experiments were very close.

Thus, we suggest summarizing the thermally induced reactions in CsB_3H_8 as follows (non-stoichiometrical):

α-CsB_3H_8 (*Ama2*) $\xrightarrow{74\,°C}$ β-CsB_3H_8 (*Pnma*) $\xrightarrow{102\,°C}$ γ-CsB_3H_8 ($Fm\bar{3}m$) $\xrightarrow{202\,°C}$ $H_2\uparrow$ + $CsBH_4$ (XRD, FTIR)…+ $Cs_xBH_4B_{10}H_{10}$ and/or $Cs_xBH_4B_6H_6$ (?, FTIR, PXRD) $\xrightarrow{520\,°C}$ gaseous boranes↑ + $Cs_2B_{12}H_{12}$ + ?.

Conclusions

In this work, we have studied two new high-temperature phases of CsB_3H_8, here named β-, and γ-CsB_3H_8. The new phases were observed by TGA-DSC measurements and *in situ* synchrotron X-ray diffraction. The structures of the two new phases, β-, and γ-CsB_3H_8, were determined by Rietveld refinement of the diffraction data as *Pnma* and *Fm-3m*. Structure refinement was supported by periodic Kohn-Sham density functional (KS-DFT) calculations. The vibrational properties of $B_3H_8^-$ were analyzed basing on the calculated spectra and on the crystal field splitting. We have found that the effect of crystal field splitting is very low but that anharmonicity and Fermi resonance effects might affect the spectra of α-CsB_3H_8. *In situ* Raman spectroscopy has demonstrated simplification of the Raman profiles. The two new phases, and in particular the γ-phase are characterized by a significant motion of the $B_3H_8^-$ units that can be of interest for solid-state ionic conductivity. The disordered motion of $B_3H_8^-$ ions was also reflected in the broadening of librational modes in the *in situ* Raman spectra.

It was confirmed, that CsB_3H_8 decomposes at 234ºC (T_{ons} = 212 °C) with the formation of crystalline $CsBH_4$, and higher boranes that at present remain unknown calling for further studies. PXRD patterns indicate the phases similar to c-$K_3BH_4B_{12}H_{12}$ but with a smaller closoborane anion whereas the FTIR data suggest the presence of $B_6H_6^{2-}$ and/or $B_{10}H_{10}^{2-}$ after the first decomposition step. FTIR spectra indicated that $Cs_2B_{12}H_{12}$ was formed only after decomposition at above 575 °C. PXRD data contain very weak peaks that could be assigned to $Cs_2B_{12}H_{12}$ suggesting a more complex phase composition. Both the FTIR and PXRD data contain unassigned peaks calling for further investigations.

We have also shown by the FTIR dehydration study that water can be removed from hydrated CsB_3H_8 upon heating below 200 °C in dynamic vacuum while cesium borates impurities decomposed at ca. 150ºC °C.

Acknowledgements

This work was financed by the European Fuel Cells and Hydrogen Joint Undertaking under collaborative project "BOR4STORE" (Grant Agreement No. 303428). We acknowledge the European Synchrotron Radiation Facility, BM01 (A and B), for provision of synchrotron radiation facilities and we would like to thank beamline scientists for the skillful assistance during the experiments.

Supplementary Material

FTIR spectra of hydrated CsB_3H_8 samples; Calculated IR and Raman spectra of α-, β-, and γ-CsB_3H_8; The CIF files of α-, β-, and γ-CsB_3H_8 for the structures obtained by Rietveld refinement and optimized using DFT.

FIGURES

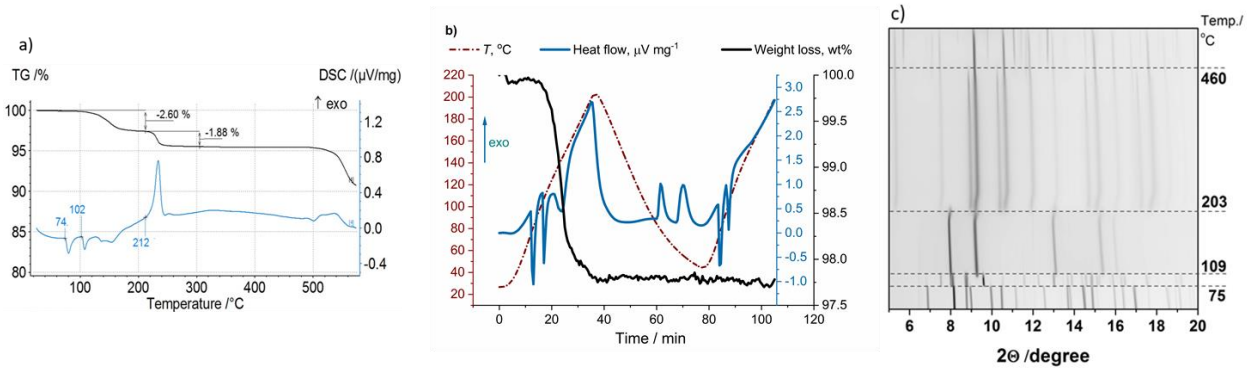

Fig. 1 DSC-TGA (a, b) and *in situ* PXRD (c) profiles of the CsB_3H_8 in 22 ─ 565 ˚C temperature range.

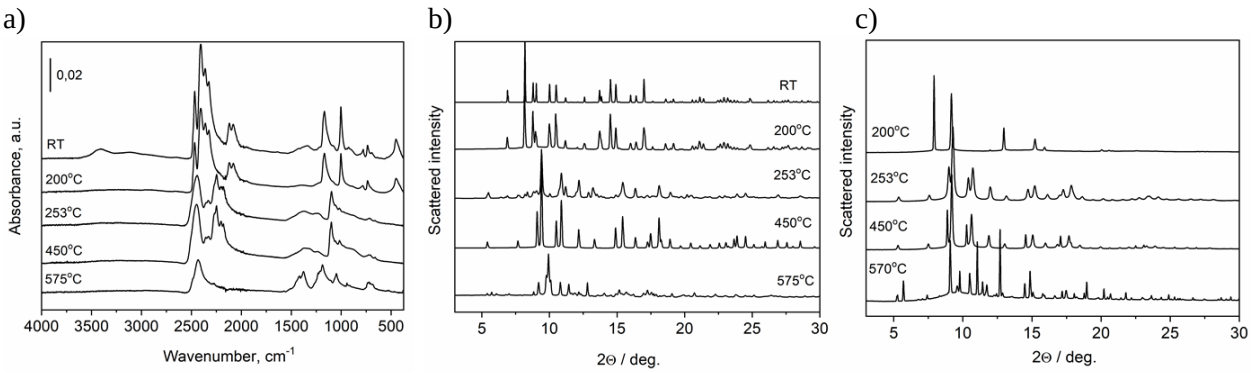

Fig. 2. (a) *Ex-situ* FTIR spectra, (b) *ex-situ* PXRD patterns of CsB_3H_8 obtained after decomposition in Ar flow at the indicated temperatures, and c) *in situ* SR-PXD patterns obtained at the indicated temperatures for a comparison with the *ex-situ* data.

a)

b)

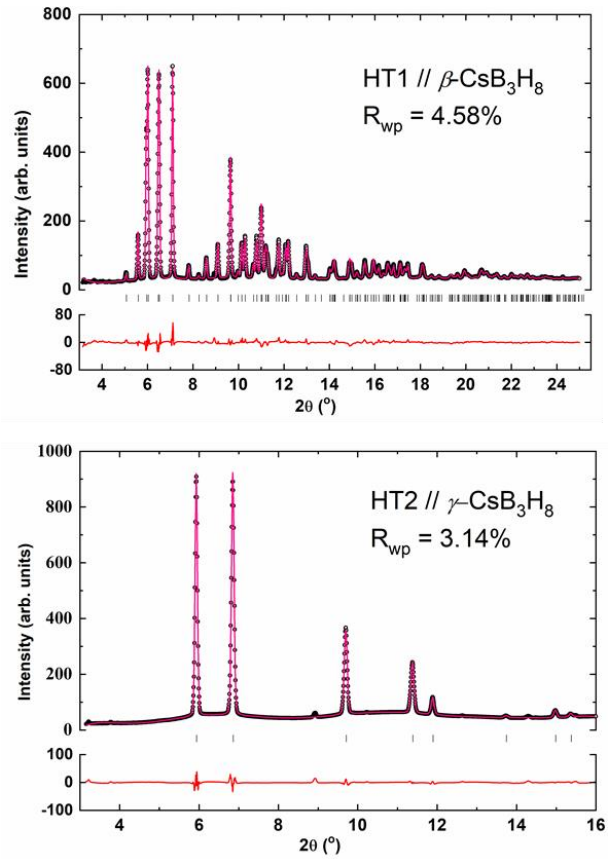

Fig. 3 The Rietveld refinements of the HT-*phase I* (β-CsB_3H_8, a) and HT-*phase II* (γ-CsB_3H_8, b).

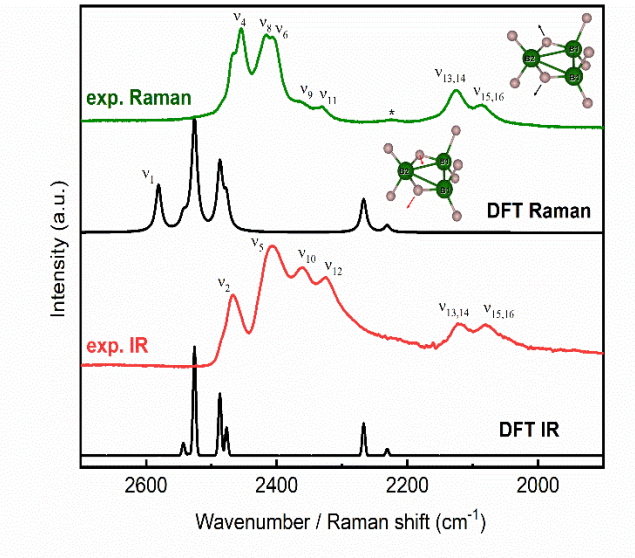

Fig. 4. Experimental and computed FTIR, Raman spectra of the R*T* phase of CsB_3H_8 (α-CsB_3H_8) in the B-H stretching region. Asterisk marks a suggested $2\nu_{27}$ mode. Structures as optimized in the periodic models at the B3LYP level (green = boron atoms; pink = hydrogen atoms). BH_{br} stretching ν_s (ν_{13}, ν_{14}) and ν_{as} (ν_{15}, ν_{16}) are illustrated by black and red arrows, respectively.

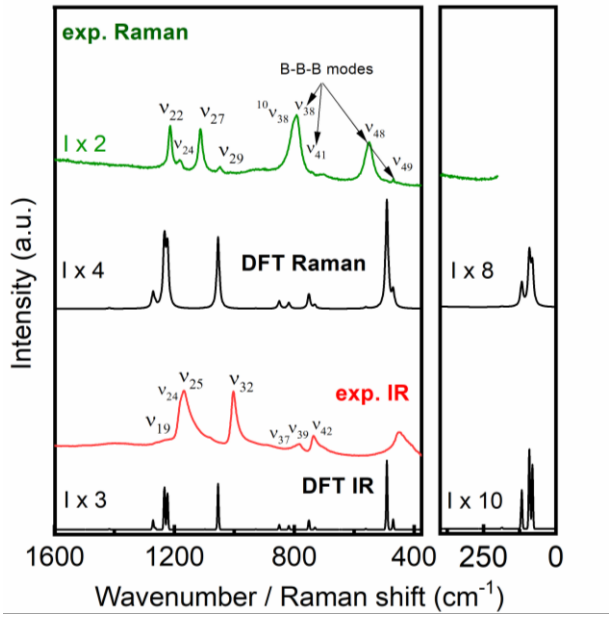

Fig. 5. Experimental and computed IR and Raman spectra of the room temperature phase of CsB_3H_8 (α-CsB_3H_8). Intensity magnification is compared to the stretching region of the relative spectra on Fig. 4.

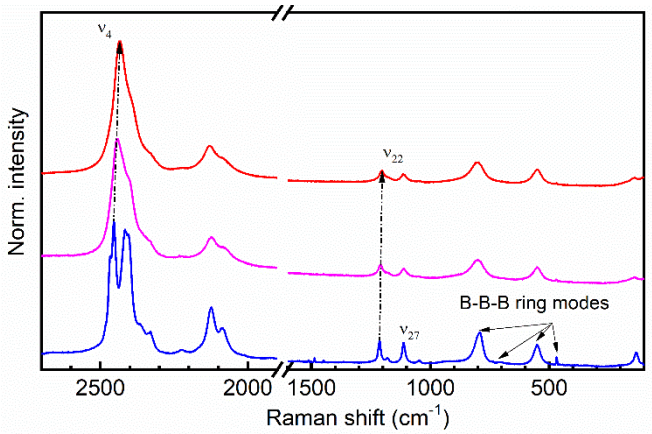

Fig. 6 Raman spectra of the *α*- (blue), *β*- (magenta), and *γ*-phases (red) of CsB_3H_8, obtained *in situ* at R*T*, 88, and 111 °C, respectively.

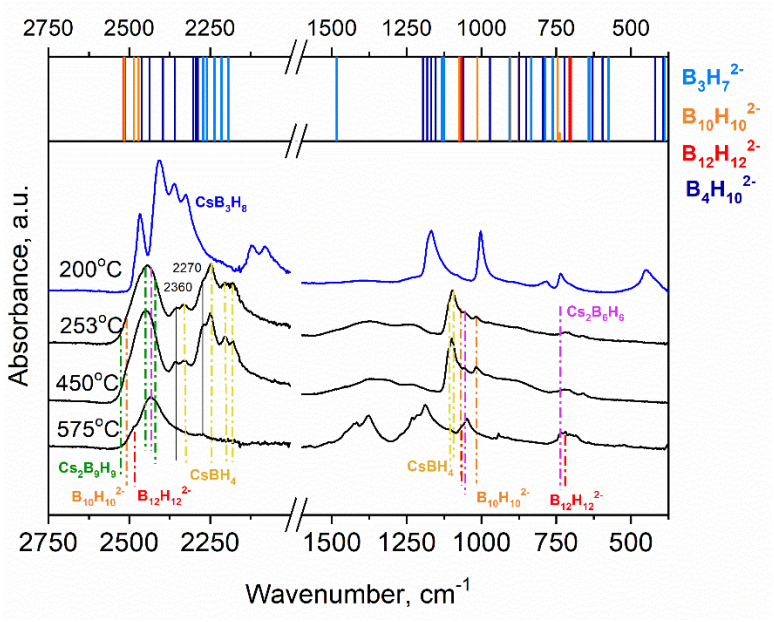

a)

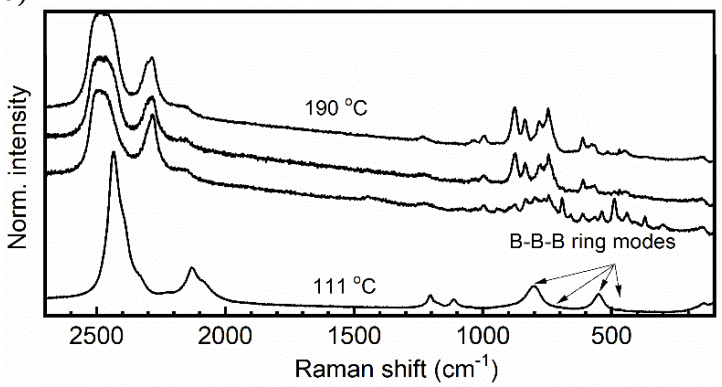

b)

Fig. 7 a) Identification of decomposition phases of CsB_3H_8 from the FTIR spectra. The spectra obtained *ex-situ* at R*T* after decomposing the sample at the indicated temperatures. Upper graph indicates the positions for the calculated IR-active modes of the BH units of possible decomposition products (values from Ref.[50]). The experimental modes with the assignment indicated with the dashed lines on the spectra are from the references [47-49]. The regions marked with asterisk is for B-O stretching and bending possibly due to the impurities;[51] b) *in situ* Raman spectra obtained with time at constant 190 °C at 25 min intervals. The bottom spectrum belongs to γ-CsB_3H_8 and is for reference.

TABLES

Table 1 Crystallographic data for CsB_3H_8 obtained by Rietveld refinement of HR-SR-PXRD data and by optimization of periodic models at the B3LYP level.

Phase data			
300 K (α-CsB_3H_8)			
	This work, exp.	This work, DFT	Ref. [25]
Crystal system	Orthorhombic	Orthorhombic	Orthorhombic
Space group	*Ama2* (no. 40)	*Ama2*	*Ama2*
Cell parameters (Å), (°)	a = 8.86567(14)	a = 8.9881	a = 8.8723(7)
	b = 8.66340(14)	b = 8.7653	b = 8.6692(7)
	c = 7.42725(13)	c = 7.4220	c = 7.4299(25)
	α = β = γ = 90	α = β = γ = 90	α = β = γ = 90
Cell volume (Å^3)	570.464(16)	584.7303	571.48
Z	4	4	4
phase I (β-CsB_3H_8)			
Crystal system	Orthorhombic	Orthorhombic	n/a
Space group	*Pnma* (no. 62)	*Pnma* (no. 62)	
Cell parameters (Å), (°)	a = 11.4197(2)	a = 11.34297	
	b = 8.87676(16)	b = 9.03894	
	c = 5.80554(11)	c = 5.75032	
	α = β = γ = 90	α = β = γ = 90	
Cell volume (Å^3)	588.505(19)	589.571	
Z	4	4	
phase II (γ-CsB_3H_8)			
Crystal system	cubic	cubic	n/a
Space group	*Fm*-3*m* (no. 225)	*Fm*-3*m* (no. 225)	
Cell parameters (Å), (°)	a = 8.44149(19)	a = 8.44100	
	α = β = γ = 90	α = β = γ = 90	
Cell volume (Å^3)	601.53(4)	601.43	
Z	4	4	

Table 2 Correlation table for the normal modes of $B_3H_8^-$ in C_{2v} crystal fields assuming C_s site symmetry [40]

Free ion symmetry, C_{2v}		Site symmetry, C_s (xz)		Crystal field splitting, C_{2v}^{16}
A_1	→	A'	→	$A_1 + B_1$
A_2	→	A''	→	$A_2 + B_2$
B_1	→	A'	→	$A_1 + B_1$
B_2	→	A''	→	$A_2 + B_2$

Table 3 Peak assignment of the experimental Raman and FTIR spectra of α-CsB_3H_8 based on the spectra calculated on the B3LYP optimized structure. All the frequencies are reported in cm^{-1}.

DFT			Experiment		Assignment
ν_i	Energy, cm^{-1}	Symmetry species	Raman	FTIR	
B-H stretching					
1,2	2581, 2579	A_1+B_1	2466 (ν_1)	2467 (ν_2)	ν_{as} (B2-H_{term})
3,4	2543, 2541	B_1+A_1	2454 (ν_4)		ν_s (B2-H_{term})
5,6	2534, 2526	B_1+A_1	2405 (ν_6)	2405 (ν_5)	$\nu_{as\text{-}in}$ (B1-H_{term})
7,8	2529, 2519	B_2+A_2	2416 (ν_8)		$\nu_{as\text{-}out}$ (B1-H_{term})
9,10	2490, 2487	A_1+B_1	2360 (ν_9)	2360 (ν_{10})	$\nu_{s\text{-}in}$ (B1-H_{term})
11,12	2486, 2477	A_2+B_2	2330 (ν_{11})	2325 (ν_{12})	$\nu_{s\text{-}out}$ (B1-H_{term})
13-14	2266, 2265	B_1+A_1	2126 (ν_{14})	2120 (ν_{13})	ν_s (BH_{br})
15-16	2223, 2218	A_2 + B_2	2086 (ν_{15})	2080 (ν_{16})	ν_{as} (BH_{br})
B-H-B bending and B-B stretching					
17-18	1418,1417	A_1+B_1			$\delta_{sci\text{-}in}$ (B-H_{term} + BH_{br})
19-20	1273,1271	A_2 +B_2		~1210 (ν_{20})	$\delta_{sci\text{-}out}$ (B-H_{term} + BH_{br})
21-22	1264,1263	B_1+A_1	1214 (ν_{22})		δ_{sci} (B-H_{term})
23-24	1232,1232	B_1+A_1	1181 (ν_{24})	1180sh (ν_{23})	δ_{sci} (B-H_{term})
25-26	1230,1222	B_2+A_2		1168 (ν_{25})	δ_{wag}(B1-H_{term}) + δ_{sci} (B2-H_{br}) + δ(BH_{br})
27-28	1171,1171	A_2+B_2	1111 (ν_{27})		δ_{twist} (B-H_{term} + BH_{br})
29-30	1098,1096	A_1+B_1	1047 (ν_{29})		δ_{twist} (B2-H_{term})
31-32	1067,1054	A_2 + B_2		1000 (ν_{32})	δ_{wag} (B2-H_{term}) + δ_{wag}(B1-H_{term})
33-34	1002,1002	A_2 + B_2			δ_{twist} (B-H_{term})
35-36	928,928	B_1+A_1			δ_{rock} (B-H_{term})
37-38	850,849	B_1+A_1	802(A_1, ^{10}B), 790 (A_1) (ν_{38})	802(ν_{37}),	ν_s (B-B-B), ring "breathing"
39-40	843,843	B_2+A_2		782(ν_{39})	δ_{rock} (B1-H_{term}) + δ_{twist} (B1-H_{term})
41-42	821,818	A_2 + B_2	739 (ν_{41})	735 (ν_{42})	ν_{as} (B-B-B)
43-44	751,750	B_1+A_1			
45-46	731,731	A_1+B_1			
47-48	561,560	B_1+A_1	550 (ν_{48})		B-B-B ring deformation
49-50	521,490	A_2 + B_2	468 (ν_{49})		B-B-B ring deformation
51-52	472,470				δ_{rock} (B1-H_{term})
53-54	249,229				δ_{rock} (B1-H_{term}) + δ_{twist} (B1-H_{term})

Table 4 Selected experimental bond distances and angles for CsB_3H_8

	α-CsB_3H_8	β-CsB_3H_8
bond distance (Å)		
B(1) – B(2)	1.779(15)	1.78(3)
B(1) – B(1)	1.807(18)	1.77(3)
B(1) – H(11)	1.22(8)	1.22(8)
B(1) – H(12)	1.23(6)	1.21(10)
B(1) – H(15)	1.27(4)	1.25(10)
B(2) – H(23)	1.24(10)	1.21(11)
B(2) – H(24)	1.20(12)	1.23(9)
B(2) – H(25)	1.44(4)	1.44(8)
bond angle (deg)		
B(2)–B(1)–B(1)	59.5(4)	60.1(1)
B(1)–B(2)–B(1)	61.0(8)	59.7(13)
H(11)–B(1)–H(12)	111(5)	117(5)
H(24)-B2-H(23)	108(8)	108(7)

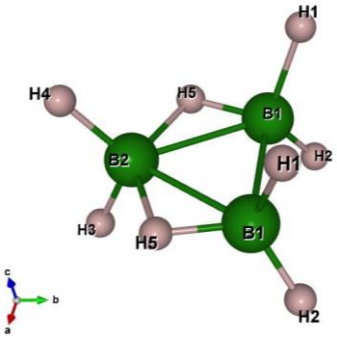

References

1. H. C. Brown, *Hydroboration*, W.A. Benjamin Inc., New York, NY, USA, 1962.
2. J. D. Clark, *Ignition!: An Informal History of Liquid Rocket Propellants*, Rutgers University Press, New Brunswick, NJ, USA, 1972.
3. L. N. Goswami, L. Ma, S. Chakravarty, Q. Cai, S. S. Jalisatgi and M. F. Hawthorne, *Inorganic Chemistry*, 2013, **52**, 1694-1700.
4. J. W. Johnson and J. F. Brody, *Journal of The Electrochemical Society*, 1982, **129**, 2213-2219.
5. R. Mohtadi and S. I. Orimo, *Nature Reviews Materials*, 2017, **2**.
6. M. Paskevicius, L. H. Jepsen, P. Schouwink, R. Cerny, D. B. Ravnsbaek, Y. Filinchuk, M. Dornheim, F. Besenbacherf and T. R. Jensen, *Chemical Society Reviews*, 2017, **46**, 1565-1634.
7. O. Zavorotynska, A. El-Kharbachi, S. Deledda and B. C. Hauback, *International Journal of Hydrogen Energy*, 2016, **41**, 14387-14403.
8. M. Chong, A. Karkamkar, T. Autrey, S. Orimo, S. Jalisatgi and C. M. Jensen, *Chemical Communications*, 2011, **47**, 1330-1332.
9. M. Chong, M. Matsuo, S. Orimo, T. Autrey and C. M. Jensen, *Inorganic Chemistry*, 2015, **54**, 4120-4125.
10. J. B. Grinderslev, K. T. Moller, Y. G. Yan, X. M. Chen, Y. T. Li, H. W. Li, W. Zhou, J. Skibsted, X. N. Chen and T. R. Jensen, *Dalton Transactions*, 2019, **48**, 8872-8881.
11. W. D. Chen, G. T. Wu, T. He, Z. Li, Z. P. Guo, H. K. Liu, Z. G. Huang and P. Chen, *International Journal of Hydrogen Energy*, 2016, **41**, 15471-15476.
12. A. Gigante, N. Leick, A. S. Lipton, B. Tran, N. A. Strange, M. Bowden, M. B. Martinez, R. Moury, T. Gennett, H. Hagemann and T. S. Autrey, *ACS Applied Energy Materials*, 2021, **4**, 3737-3747.
13. M. Matsuo, Y. Nakamori, S. Orimo, H. Maekawa and H. Takamura, *Applied Physics Letters*, 2007, **91**.
14. K. Takahashi, K. Hattori, T. Yamazaki, K. Takada, M. Matsuo, S. Orimo, H. Maekawa and H. Takamura, *Journal of Power Sources*, 2013, **226**, 61-64.
15. H. Maekawa, M. Matsuo, H. Takamura, M. Ando, Y. Noda, T. Karahashi and S. I. Orimo, *Journal of the American Chemical Society*, 2009, **131**, 894-+.
16. L. H. Rude, O. Zavorotynska, L. M. Arnbjerg, D. B. Ravnsbaek, R. A. Malmkjaer, H. Grove, B. C. Hauback, M. Baricco, Y. Filinchuk, F. Besenbacher and T. R. Jensen, *International Journal of Hydrogen Energy*, 2011, **36**, 15664-15672.
17. O. Zavorotynska, M. Corno, E. Pinatel, L. H. Rude, P. Ugliengo, T. R. Jensen and M. Baricco, *Crystals*, 2012, **2**, 144-158.
18. S. Kim, H. Oguchi, N. Toyama, T. Sato, S. Takagi, T. Otomo, D. Arunkumar, N. Kuwata, J. Kawamura and S. Orimo, *Nat. Commun.*, 2019, **10**, 9.
19. R. Černý, M. Brighi and F. Murgia, *Chemistry*, 2020, **2**, 805-826.
20. A. C. Dunbar, J. A. Macor and G. S. Girolami, *Inorganic Chemistry*, 2014, **53**, 822-826.
21. Z. G. Huang, M. Eagles, S. Porter, E. G. Sorte, B. Billet, R. L. Corey, M. S. Conradi and J. C. Zhao, *Dalton Transactions*, 2013, **42**, 701-708.
22. S. N. Li, H. Quan and S. Y. Yu, *Solid State Communications*, 2019, **299**.
23. X. M. Chen, N. N. Ma, X. R. Liu, C. G. Wei, C. C. Cui, B. L. Cao, Y. H. Guo, L. S. Wang, Q. F. Gu and X. N. Chen, *Angewandte Chemie-International Edition*, 2019, **58**, 2720-2724.
24. M. S. Andersson, J. B. Grinderslev, X. M. Chen, X. Chen, U. Häussermann, W. Zhou, T. R. Jensen, M. Karlsson and T. J. Udovic, *The Journal of Physical Chemistry C*, 2021, **125**, 3716-3724.
25. H. J. Deiseroth, O. Sommer, H. Binder, K. Wolfer and B. Frei, *Zeitschrift Fur Anorganische Und Allgemeine Chemie*, 1989, **571**, 21-28.

26. J. Tomkinson, C. J. Ludman and T. C. Waddington, *Spectrochimica Acta Part A: Molecular Spectroscopy*, 1979, **35**, 117-122.
27. A. A. Coelho, *Journal of Applied Crystallography*, 2018, **51**, 210-218.
28. R. Dovesi, A. Erba, R. Orlando, C. M. Zicovich-Wilson, B. Civalleri, L. Maschio, M. Rérat, S. Casassa, J. Baima, S. Salustro and B. Kirtman, *WIREs Comput Mol Sci.*, 2018, **8**, e1360.
29. A. D. Becke, *J. Chem. Phys.*, 1993, **98**, 5648-5652.
30. C. Lee, W. Yang and R. G. Parr, *Phys. Rev. B*, 1988, **37**, 785-789.
31. I. S. Lim, P. Schwerdtfeger, B. Metz and H. Stoll, *The Journal of Chemical Physics*, 2005, **122**, 104103.
32. Energy-consistent Pseudopotentials of the Stuttgart/Cologne Group, http://www.tc.uni-koeln.de/PP/clickpse.en.html, (accessed February 18th, 2020).
33. R. Dovesi, R. Orlando, A. Erba, C. M. Zicovich-Wilson, B. Civalleri, S. Casassa, L. Maschio, M. Ferrabone, M. De La Pierre, P. D'Arco, Y. Noel, M. Causa, M. Rerat and B. Kirtman, *Int. J. Quantum Chem.*, 2014, **114**, 1287-1317.
34. C. G. Broyden, *Math. Comput.*, 1965, **19**, 577–593.
35. D. D. Johnson, *Physical Review B*, 1988, **38**, 12807-12813.
36. F. Pascale, C. M. Zicovich-Wilson, F. López Gejo, B. Civalleri, R. Orlando and R. Dovesi, *J. Comput. Chem.*, 2004, **25**, 888-897.
37. L. Maschio, B. Kirtman, M. Rérat, R. Orlando and R. Dovesi, *The Journal of Chemical Physics*, 2013, **139**, 164102.
38. L. Maschio, B. Kirtman, M. Rérat, R. Orlando and R. Dovesi, *The Journal of Chemical Physics*, 2013, **139**, 164101.
39. W. N. Lipscomb, *Adv. Inorg. Chem. Radiochem.*, 1959, **1**, 117.
40. K. Nakamoto, *Infrared and Raman Spectra of Inorganic and Coordination Compounds*, 6th edn., 2008.
41. M. I. Aroyo, A. Kirov, C. Capillas, J. M. Perez-Mato and H. Wondratschek, *Acta Crystallographica Section A*, 2006, **62**, 115-128.
42. P. Carbonnière and H. Hagemann, *The Journal of Physical Chemistry A*, 2006, **110**, 9927-9933.
43. O. Zavorotynska, M. Corno, A. Damin, G. Spoto, P. Ugliengo and M. Baricco, *Journal of Physical Chemistry C*, 2011, **115**, 18890-18900.
44. S. F. Parker, *Coordination Chemistry Reviews*, 2010, **254**, 215-234.
45. S. Kirklin, J. E. Saal, B. Meredig, A. Thompson, J. W. Doak, M. Aykol, S. Rühl and C. Wolverton, *npj Computational Materials*, 2015, **1**, 15010.
46. J. E. Saal, S. Kirklin, M. Aykol, B. Meredig and C. Wolverton, *JOM*, 2013, **65**, 1501-1509.
47. P. Brint, B. Sangchakr, P. W. Fowler and V. J. Weldon, *J. Chem. Soc.-Dalton Trans.*, 1989, DOI: 10.1039/dt9890002253, 2253-2260.
48. L. A. Leites, *Chem. Rev.*, 1992, **92**, 279-323.
49. G. Renaudin, S. Gomes, H. Hagemann, L. Keller and K. Yvon, *J. Alloy. Compd.*, 2004, **375**, 98-106.
50. J. G. Vitillo, S. Bordiga and M. Baricco, *Journal of Physical Chemistry C*, 2015, **119**, 25340-25351.
51. J. Li, S. P. Xia and S. Y. Gao, *Spectroc. Acta Pt. A-Molec. Biomolec. Spectr.*, 1995, **51**, 519-532.